Tunable topological semimetal states with ultraflat nodal rings in strained YN

Huaqing Huang,[1] Wei Jiang,[1] Kyung-Hwan Jin,[1] and Feng Liu[1,2]
[1]*Department of Materials Science and Engineering, University of Utah, Salt Lake City, Utah 84112, USA*
[2]*Collaborative Innovation Center of Quantum Matter, Beijing 100084, China*

(Received 20 April 2018; published 23 July 2018)

Using first-principles calculations and effective model analysis, we demonstrate that the strained WC-type YN can host an ideal topological semimetal state with an ultraflat nodal ring in the absence of spin-orbit coupling. Distinguished from previous nodal-line semimetals, the nodal ring in YN lies in a single plane of the Brillouin zone with an energy variation less than 0.3 meV; that is, the nodal ring is flat in both momentum and energy space. Interestingly, by applying a uniaxial strain along the c axis, one can effectively tune the size of the nodal ring and even realize a topological phase transition from nodal-ring semimetals to normal insulators. The nodal ring here is topologically nontrivial, as confirmed by directly calculating the topological invariant and topological drumhead surface state. Moreover, due to an anisotropic torus Fermi surface and the nontrivial topology, exotic magnetoresponse effects, including anomalous Landau level structures and direction-dependent phase shifts of quantum oscillations with and without a Berry phase of π, can be probed experimentally.

DOI: 10.1103/PhysRevB.98.045131

I. INTRODUCTION

Since the remarkable discovery of topological insulators [1,2], the study of electronic structure topology of crystalline materials has emerged as a major new theme in condensed-matter physics and material science. Recently, the focus has shifted towards topological semimetals. The topological semimetallic states are characterized by band crossing (BC) points or lines between conduction and valence bands in three-dimensional (3D) momentum space. The Weyl (Dirac) semimetals have isolated twofold (fourfold) degenerate BC points near the Fermi level, while the nodal-line semimetals possess one-dimensional (1D) lines of BC points around the Fermi level. Consequently, the Fermi surfaces of topological semimetals are distinct from conventional metals. The topological semimetals can be further classified into different types by fermiology. For example, type-I Dirac/Weyl semimetals have a pointlike Fermi surface [3–7], type-II Dirac/Weyl semimetals possess both electron and hole pockets that contact at the type-II Dirac/Weyl point [8–12], and type-III Dirac/Weyl semimetals have a unique linelike Fermi surface [13]. For nodal-line semimetals, the classification is much more complicated. Nodal-line semimetals have been classified into type I/II based on the band tilting around the nodal line [14–18] or type A/B according to the position and shape of nodal lines [19,20]. Due to different number, distribution, and/or connection of nodal lines, even more complicated nodal structures are formed in momentum space which lead to various new types of nodal-line semimetals, including nodal-net [21–24], nodal-chain [25–27], nodal-link [28–30], nodal-knot [31], and nodal-sphere [32] semimetals.

On the other hand, because of the energy variation along the nodal line, nodal-line semimetals with similar nodal structures can have different Fermi surfaces, which leads to distinctive physical properties. When a nodal-line semimetal is protected by a mirror symmetry, the nodal line lies in a mirror plane of the Brillouin zone (BZ), which means it is flat in momentum space. However, the nodal line is not constrained to occur on a constant energy contour. An energy variation along the nodal line has no effect on the topological character of the nodal line. But it generally drives the system into a semimetallic state with coexisting electron and hole pockets, which makes some nodes in the nodal line become electron and hole pocket contacting (EHPC) points. More importantly, the resultant unconventional Fermi surface geometry would significantly change the optical and magnetic response of the nodal-line semimetals. For example, the optical conductivity of such nodal lines exhibits new spectral features that occur as a result of the Dupin cyclide geometry of the Fermi surface manifesting the energy dispersion along the nodal line [33–36]. Different Fermi surfaces also lead to distinct features in the Landau level distribution which affect the behaviors of magnetic quantum oscillations [37–40]. We therefore propose a further classification of the nodal-line semimetals into two types, i.e., energetically flat versus dispersive nodal lines by fermiology, which can be realized by counting the number of EHPC points in the nodal line. As shown in Fig. 1, the flat nodal-line semimetals have no EHPC points in the entire nodal line, meaning that the whole nodal line is encapsulated by either an electron or a hole pocket. The dispersive nodal-line semimetals have discrete EHPC points in the nodal line, which means a Fermi surface composed of both electron and hole pockets contacting at some nodes of the nodal line. Of course, the number of EHPC points depends on the relative position of the chemical potential μ and the energy variation of the nodal line. Therefore, by doping or gating, one can tune the Fermi surface geometry (the so-called Lifshitz transition) and even realize the transition between an energetically flat nodal line without EHPC points and a dispersive nodal line with discrete EHPC points, resulting in physically observable quantities in optical and magnetic response experiments.

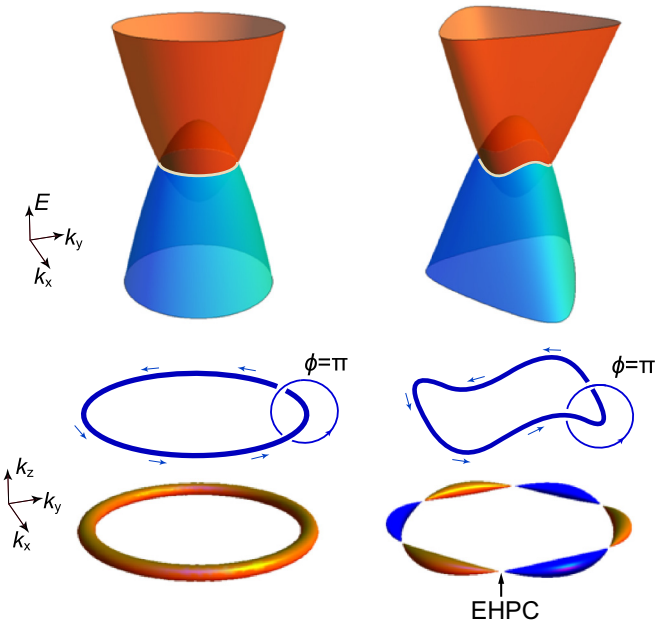

FIG. 1. Schematic illustration of the energetically flat and dispersive nodal-line semimetals without and with energy variation along the nodal line.

In this work, we discover that the strained WC-type YN is an ideal topological semimetal with an ultraflat nodal ring around the center of the BZ when spin-orbit coupling (SOC) is absent. The nodal ring lies in a mirror plane in momentum space with a negligible energy variation along the ring. The radius of the nodal ring can be tuned and a topological phase transition can be realized by an external uniaxial strain along the c axis. The nontrivial topological nature of the nodal ring is demonstrated by calculating the topological invariant and topological drumhead surface state. Moreover, we further studied the magnetoresponse effect of YN and found anomalous Landau level structures and direction-dependent phase shifts of quantum oscillations. Our finding provides a prototype material candidate to investigate novel magnetoresponse properties solely induced by a nodal ring associated with unconventional Fermi surfaces.

II. MODEL AND METHODS

YN belongs to a large family of transition-metal nitrides, which have different structures [41]. The YN studied here has a WC-type hexagonal crystal structure with space group $P\bar{6}m2$ (D^1_{3h}, No. 187), as shown in Fig. 2 [42]. Y and N atoms are located at the 1d (1/3, 2/3, 1/2) and 1a (0, 0, 0) Wyckoff positions, respectively. The calculated lattice constants are $a = b = 3.337$ Å and $c = 3.040$ Å. The basic symmetries of this structure are listed in Table I. The calculated total energy of the WC-type YN is just tens of to a few hundred millielectron volts per atom higher than that of other allotropes, indicating that the WC-type YN is metastable but likely experimentally accessible.

The first-principles calculations are performed within the framework of density functional theory using the projector augmented-wave method [43] as implemented in the Vienna

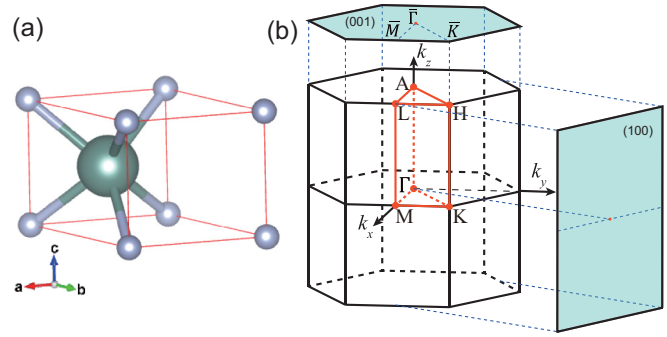

FIG. 2. (a) Atomic structure of YN with $P\bar{6}m2$ (No. 187) symmetry. (b) The first BZ of YN, with the high-symmetry points and lines highlighted in red. The semitransparent green planes indicate the projected surface BZ of the (001) and (100) surfaces.

Ab initio Simulation Package (VASP) [44]. The generalized gradient approximation was adopted with the Perdew-Burke-Ernzerhof-type exchange-correlation functional [45]. All the calculations are carried out using a kinetic-energy cutoff of 400 eV on the 10×10×10 Γ-centered **k**-point mesh. The surface state is calculated using a tight-binding Hamiltonian based on Wannier functions, which are constructed by projecting bulk Bloch wave functions into Y d and N p orbitals [46].

III. RESULTS AND DISCUSSION

A. Band structure

The band structures calculated without SOC are presented in Fig. 3(a), which clearly shows that two band crossings along Γ-M and Γ-K exist exactly at the Fermi level. Further orbital-character analysis reveals that these two crossing bands in Fig. 3(a) around the Fermi level are mainly contributed by Y d_{z^2} and N p_z orbitals, which are symmetric and antisymmetric under M_{001} mirror reflection, respectively. Since the conduction and valence bands have opposite parities with respect to the M_{001} mirror symmetry, the band crossing between these two bands does not just appear at two discrete points on the Γ-M and Γ-K lines but also persists along a closed loop on the $k_z = 0$ plane, forming a nodal ring around the Γ point. The radius of the nodal ring is about 0.15 Å^{-1}, which can be observed by angle-resolved photoemission spectroscopy. Moreover, the band crossings also show a clear signature of band inversion at Γ, implying the nontrivial band topology of this system, as discussed later.

Interestingly, we found that the nodal ring lies exactly at the Fermi level without energy variation. Therefore, the Fermi surface is just a circle coinciding with the nodal ring. The

TABLE I. Symmetry generators of the space group $P\bar{6}m2$ (No. 187) for YN.

Symmetry	(x, y, z) form	Operation
Identify	(x, y, z)	$\{1\|0\}$
Rotation	$(-y, x-y, z)$	$\{3^+_{001}\|0\}$
Mirror	$(x, y, -z)$	$\{M_{001}\|0\}$
Mirror	$(-y, -x, z)$	$\{M_{110}\|0\}$

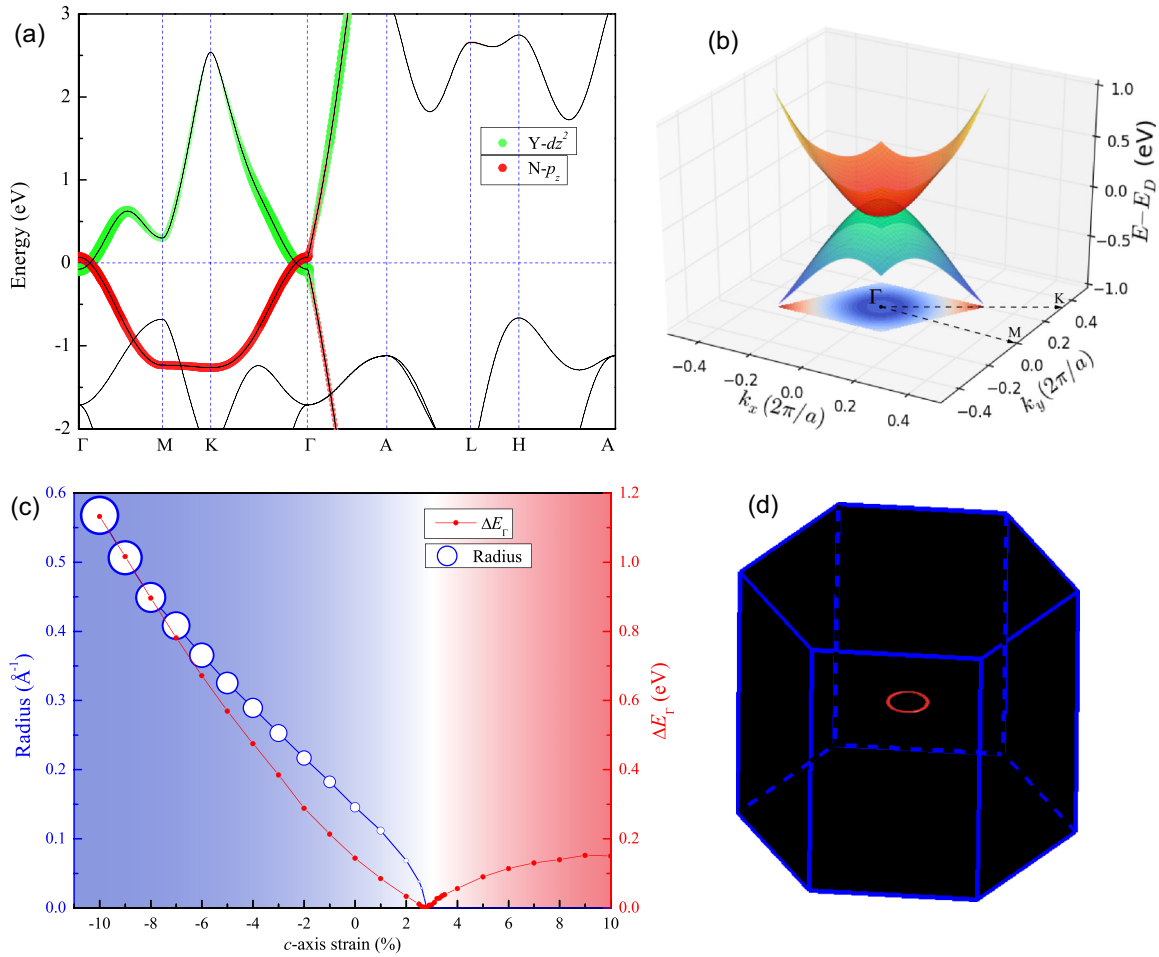

FIG. 3. (a) Band structure of YN along the high-symmetry lines of the Brillouin zone without SOC. Red and green dots in band structures indicate the projection onto the N p_z and Y d_{z^2} orbitals, respectively. (b) The 3D plot of the band structure around the Fermi level. The bottom projection shows the isoenergy contour of the energy difference between the conduction and valence bands. (c) The radius of the nodal ring and the energy gap at Γ (ΔE_Γ) as a function of uniaxial strain along the c axis. (d) The 3D isoenergy surface of YN at $E_F + 15$ meV, where a torus electron pocket locates around the center of the BZ.

shape of the nodal ring can also be easily inferred from an isoenergy contour at an energy slightly departing from the Fermi energy E_F. As shown in Fig. 3(d), one isoenergy contour is plotted at 15 meV above the Fermi surface of YN, which would shrink exactly to the nodal ring in the $k_z = 0$ plane, forming a perfect torus winding around the Γ point. To reveal the energy dispersion of the nodal ring, we calculated the 3D band structure around the Γ point, as shown in Fig. 3(b). We found that the whole ring lies almost in the same energy within an energy variation less than 0.3 meV, indicating that the nodal ring is ultraflat in both energy and momentum space. Further fine calculations show that the linearly dispersive conduction and valence bands around the nodal ring are symmetric with respect to the Fermi level, exhibiting a perfect low-energy particle-hole symmetry of the electronic structure. This is because the systems are bipartite, with two interpenetrating sublattices of Y and N, so the band structures are symmetric about the Fermi level.

We next studied the effect of uniaxial strains along the c axis on the nodal ring of YN. As shown in Fig. 3(c), we found that the size of the nodal ring can be effectively enlarged by applying a compressive uniaxial strain. More interestingly, a topological phase transition from a topological nodal-ring semimetal to a normal insulator can be realized by a tensile strain. The energy gap at Γ (ΔE_Γ) first decreases rapidly with the increasing tensile strain and then increases after a critical strain of about 2.8%. This indicates that a band inversion occurs at the phase-transition point. The system then becomes a normal insulator without a nodal ring at the Fermi level. Such a strong effect of the c-axis strains on the electronic structure of YN is due to the fact that two crossing bands are composed of Y d_{z^2} and N p_z orbitals, which have a strong response to the c-axis strain. With the c-axis strains, the relative energy level of the two orbitals changes, which leads to the variation of the band crossing between the conduction and valence bands. We also checked the strain effect using the nonlocal Heyd-Scuseria-Ernzerhof (HSE06) hybrid functional calculation [47,48] and found that the phase transition occurs under a compressive strain of about −7.5%. Additionally, the unique ultraflat nodal ring still exists in the semimetal phase (see Appendix A). We therefore expected that the exact strain of the critical transition point could be determined by

experiments. We also studied the effect of uniaxial strains along the a or b axis on the nodal ring of YN. We found that the nodal ring, although it becomes elliptical, persists under in-plane uniaxial strain. This is because the a- or b-axis strain does not break the M_{001} mirror symmetry which protects the existence of the nodal ring in the k_x-k_y plane.

B. Effective $k\cdot p$ Hamiltonian

We construct an effective model to describe the nodal ring around the Γ point by considering the symmetry constraints of the Hamiltonian. A minimal $k\cdot p$ Hamiltonian for the two crossing bands around Γ can be written as

$$H(\mathbf{k}) = d_0(\mathbf{k})\sigma_0 + \mathbf{d}(\mathbf{k})\cdot\boldsymbol{\sigma}, \tag{1}$$

where the 2×2 identity matrix σ_0 and Pauli matrices $\boldsymbol{\sigma} = (\sigma_x, \sigma_y, \sigma_z)$ operate in the pseudospin space of the two crossing bands and $d_0(\mathbf{k})$ and $\mathbf{d}(\mathbf{k}) = (d_x(\mathbf{k}), d_y(\mathbf{k}), d_z(\mathbf{k}))$ are real functions of $\mathbf{k} = (k_x, k_y, k_z)$. We ignore $d_0(\mathbf{k})$, which represents an insignificantly small overall energy shift, because the nodal line is ultraflat in YN, so it is irrelevant in studying the band crossing. The symmetry at Γ is characterized by the D_{3h} symmetry group, which contains a threefold rotation C_3 about k_z, mirror reflections M_{001} and M_{110} (see Table I), and time-reversal symmetry T. These symmetries impose the following constraints on the Hamiltonian:

$$C_3 H(\mathbf{k}) C_3^{-1} = H\left(-\tfrac{k_x+\sqrt{3}k_y}{2}, \tfrac{\sqrt{3}k_x-k_y}{2}, k_z\right), \tag{2}$$

$$M_{001} H(\mathbf{k}) M_{001}^{-1} = H(k_x, k_y, -k_z), \tag{3}$$

$$M_{110} H(\mathbf{k}) M_{110}^{-1} = H(k_x, -k_y, k_z), \tag{4}$$

$$T H(\mathbf{k}) T^{-1} = H(-k_x, -k_y, -k_z). \tag{5}$$

The bands around the Fermi level are mainly contributed by Y d_{z^2} and N p_z. If we choose the two basis vectors to be $|d_{z^2}\rangle$ and $|p_z\rangle$, the symmetry operations take the form $C_3 = \sigma_0$, $M_{001} = \sigma_z$, $M_{110} = \sigma_0$, and $T = K\sigma_0$, where K is the complex-conjugation operator. Then these symmetry constraints allow the following form of $\mathbf{d}(\mathbf{k})$:

$$C_3: \quad d_{x,y,z}(\mathbf{k}) = d_{x,y,z}\left(-\tfrac{k_x+\sqrt{3}k_y}{2}, \tfrac{\sqrt{3}k_x-k_y}{2}, k_z\right), \tag{6}$$

$$M_{001}: \quad -d_{x,y}(\mathbf{k}) = d_{x,y}(k_x, k_y, -k_z), \tag{7}$$

$$d_z(\mathbf{k}) = d_z(k_x, k_y, -k_z), \tag{8}$$

$$M_{110}: \quad d_{x,y,z}(\mathbf{k}) = d_{x,y,z}(k_x, -k_y, k_z), \tag{9}$$

$$T: \quad d_{x,z}(\mathbf{k}) = d_{x,z}(-k_x, -k_y, -k_z), \tag{10}$$

$$d_y(\mathbf{k}) = -d_y(-k_x, -k_y, -k_z). \tag{11}$$

Thus, we can obtain the symmetry-allowed expressions for $\mathbf{d}(\mathbf{k})$:

$$d_x(\mathbf{k}) = 0, \tag{12}$$

$$d_y(\mathbf{k}) = a_1 k_z + a_2 k_z\left(k_x^2 + k_y^2\right) + a_3 k_z^3, \tag{13}$$

$$d_z(\mathbf{k}) = m_0 + m_1\left(k_x^2 + k_y^2\right) + m_2 k_z^2, \tag{14}$$

up to the third order of $\mathbf{k}$. The parameters a_i and m_i in the above Hamiltonian can be determined by fitting the energy spectrum of the effective Hamiltonian $\epsilon_\pm = d_0(\mathbf{k}) \pm \sqrt{d_y(\mathbf{k})^2 + d_z(\mathbf{k})^2}$ to that of the first-principles calculations. Since there is a band inversion around Γ in the k_x-k_y plane, $m_0 m_1 < 0$ is satisfied, which is nothing but the condition for the existence of a nodal ring, as shown in the following.

It is noted that the above Hamiltonian is expressed only in terms of two out of the three Pauli matrices. Hence, the codimension of a band crossing problem is 2, one less than the number of independent variables (i.e., k_x, k_y, and k_z), and then a nodal ring should be stable in this system [49]. The band crossing points can be obtained by solving $d_y(k) = 0$ and $d_z(k) = 0$. According to Eqs. (12)–(14), d_y vanishes on the $k_z = 0$ plane. Therefore, the solution $d_z(k_x, k_y, 0) = m_0 + m_1(k_x^2 + k_y^2) = 0$ determines the band crossing points which form a ring in the $k_z = 0$ plane with a radius of $\sqrt{-m_0/m_1}$.

C. Topological invariant and drumhead surface state

To identify the nontrivial topology of YN, we calculated the topological invariant ζ_1, which is defined on a closed path C wrapped around the nodal ring [50]. The expression of ζ_1 is given by

$$\zeta_1 = \frac{\phi_B}{\pi} = \frac{1}{\pi}\oint_C d\mathbf{k}\cdot\mathcal{A}(\mathbf{k}), \tag{15}$$

where $\mathcal{A}(\mathbf{k}) = i\sum_n \langle u_n(\mathbf{k})|\nabla_{\mathbf{k}}|u_n(\mathbf{k})\rangle$ is the Berry connection. With the effective Hamiltonian in Eqs. (12)–(14), we obtained the topological invariant $\zeta_1 = 1$ for any path in the BZ that goes around the nodal ring (see Appendix B). This indicates that the nodal ring is topologically stable against perturbations.

One of the characteristic signatures of a topological nodal-line semimetal is the existence of drumhead surface states [49,51]. To further reveal the nontrivial topological nature of YN, we calculated the (001) surface states for a Y-terminated semi-infinite system using an iterative surface Green's function method [52–54] based on the tight-binding model. As shown in Fig. 4(a), the surface states connect two gapless points, which are the projections of the nodal points. Such a surface state is the so-called drumhead surface state, which is nestled inside of the projected nodal ring with a bandwidth of about 55 meV. Interestingly, when the (001) surface is terminated on the N atomic layer, the topological surface state occupies a region outside the projected nodal ring, exactly the opposite to the Y-terminated surface. The Fermi surface of the (001) surface shows a clear circular pattern which is just the projection of the bulk nodal ring [Fig. 4(b)]. Also, the projected Fermi surface on the side surface, i.e., the (100) surface, is a piece of a straight line [see Fig. 4(c)], implying that the bulk nodal ring lies flat in the k_x-k_y plane.

D. Effect of spin-orbit coupling

The SOC effect can drive the nodal-line semimetal into different topological states [55–57], including topological insulators [49,51], Dirac semimetals [22,23], and different kinds of nodal-line semimetals [58–60]. When SOC is considered here, the nodal ring is gapped, and the system becomes a topological insulator with a topological invariant $Z_2 = (1; 000)$.

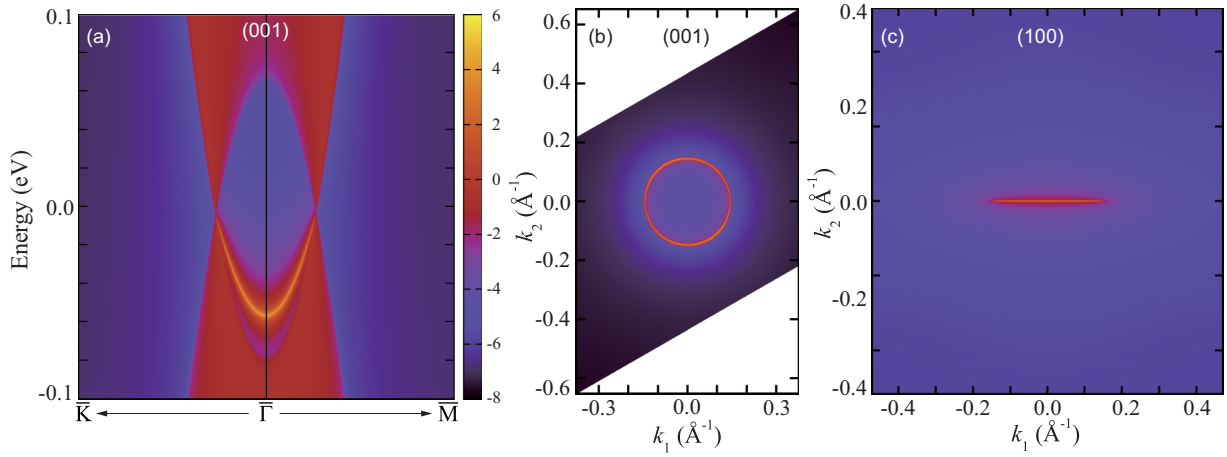

FIG. 4. (a) Calculated (001) surface spectrum for a Y-terminated semi-infinite YN system. The nontrivial topological surface states connecting the surface projection of bulk nodal points are clearly visible. (b) The Fermi surface of the (001) surface. (c) The Fermi surface of the (100) surface.

More detailed band-structure calculations using the Wannier interpolation indicate that the SOC-induced gap along the nodal ring is only about 4.0 meV (see Fig. 5), which is much smaller than the bandwidth of the surface state. Therefore, although SOC would lift the degenerate drumhead surface state slightly, the SOC-induced splitting of the surface state is effectively negligible.

Another effect of SOC is that the conduction and valence bands along Γ-A are split and several triply degenerate points appear, as shown in the inset of Fig. 5. This is similar to the case of recently found topological triple-point metals with the same crystal symmetry [61–67]. The position and energy of all the triply degenerate points are listed in Table II. It is worth noting that the triple points in the valence bands are mainly composed of p orbitals, while those on conduction bands are contributed by d orbitals. Therefore, both p- and d-electron-mediated triple-point fermions can be realized in YN. However, as these triply degenerate points are about −1.5 eV below or 3.5 eV above the Fermi level, they can hardly be detected experimentally.

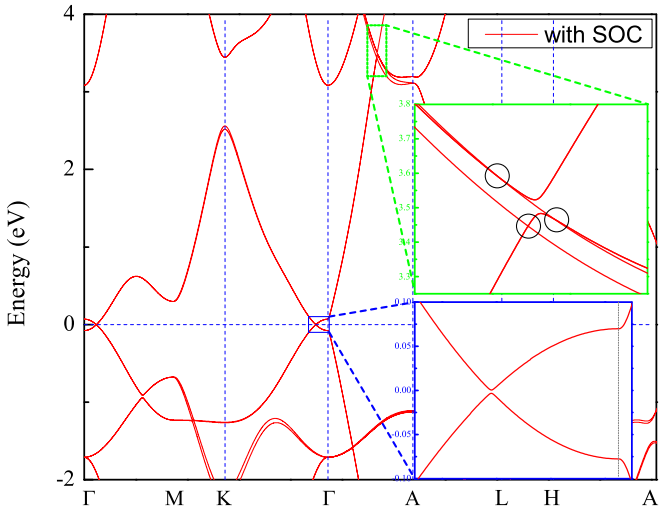

FIG. 5. Band structure of YN along the high-symmetry lines of the Brillouin zone in the presence of SOC. The insets show zoomed-in plots of band structures around the gapped nodal ring (blue box) and triple points (green box), respectively. The triply degenerate points are denoted by the black circles in the inset.

E. Magnetoresponse effect

Topological semimetals show interesting magnetoresponse effects. For example, Weyl and Dirac semimetals exhibit the chiral anomaly effect [68] which manifests as a large negative longitudinal magnetoresistance [69–73]. A nontrivial Berry phase of π can be probed by the quantum oscillation in two-dimensional (2D) and 3D Dirac materials such as graphene [74,75] and Cd_3As_2 [76,77]. Given the ideal nodal ring of YN, interesting features of magnetoresponse effects can be observed to manifest its anisotropic torus Fermi surface and nontrivial topology [37].

As an example, we apply a magnetic field along the z axis, $\mathbf{B}_\perp = (0, 0, B)$ and choose the Landau gauge so that the vector potential is $\mathbf{A} = (-yB, 0, 0)$. Using the Peierls substitution method, we calculated the Hamiltonian under the magnetic field by replacing $\mathbf{k}$ with $(k_x - eyB/\hbar, -i\partial_y, k_z)$. Neglecting the insignificant tiny third-order terms, the effective magnetic Hamiltonian is written as

$$H_{\mathbf{B}_\perp} = \left[\hbar\omega(b^\dagger b + 1/2) + m_2 k_z^2 + m_0\right]\sigma_z + a_1 k_z \sigma_y, \quad (16)$$

TABLE II. Position k_z and energy E_T of triply degenerate points along Γ-A.

k_z (units of $2\pi/c$)	E_T (eV)
0.1361	−1.598
0.2533	−1.378
0.1488	−1.570
0.2878	3.449
0.2978	3.467
0.2763	3.587

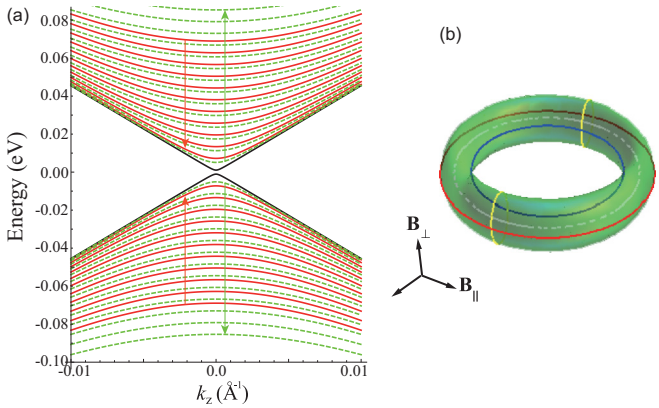

FIG. 6. (a) The Landau levels for the nodal-ring semimetal in a perpendicular magnetic field $\mathbf{B}_\perp$. The parameters are $m_0 = -0.072\,\text{eV}$, $m_1 = 3.386\,\text{eV Å}^2$, $m_2 = -7.282\,\text{eV Å}^2$, $a_1 = 4.543\,\text{eVÅ}$, and $B = 60$ T. The upper magnetic Landau levels go downward first (red arrow) and then go upward (green arrow) with the increase in Landau index n. The black line represents the critical Landau level $\bar{n}$. The red solid lines (green dashed lines) indicate Landau levels with $n < \bar{n}$ ($n > \bar{n}$). (b) Schematic illustration of the extremal cyclotron orbits on the torus Fermi surface (green). The white dashed line stands for the nodal ring. The red and blue circles represent maximum and minimum cross sections of the torus Fermi surface in a perpendicular magnetic field $\mathbf{B}_\perp$. The yellow rings represent extremal cross sections of the torus Fermi surface in a parallel magnetic field $\mathbf{B}_\parallel$.

where $\omega = 2eBm_1/\hbar^2$ is the cyclotron frequency and $b = -[(y - l_B^2 k_x)/l_B + l_B\partial_y]/\sqrt{2}$ and $b^\dagger = -[(y - l_B^2 k_x)/l_B - l_B\partial_y]/\sqrt{2}$ are the ladder operators with the magnetic length $l_B = \sqrt{\hbar/eB}$. The eigenvalues of the system in the presence of magnetic field $\mathbf{B}_\perp$ are given by

$$E^\pm(n, k_z) = \pm\sqrt{\left[\hbar\omega(n + 1/2) + m_2 k_z^2 + m_0\right]^2 + a_1^2 k_z^2}. \tag{17}$$

Let us focus on the bottom parts of the electron Landau bands where $k_z = 0$. Then the Landau levels are simplified to

$$E^\pm(n, 0) = \pm|\hbar\omega(n + 1/2) + m_0|. \tag{18}$$

Because of the band inversion around Γ, m_0 and $\hbar\omega = 2m_1/l_B^2$ have opposite signs. For a magnetic field $B < -m_0 m_1 \hbar/e$, the upper magnetic subbands go downward first and then go upward with the increase in Landau index n, as shown in Fig. 6(a). The critical Landau level is around $\bar{n} = \text{Int}[-(m_0/\hbar\omega + 1/2)]$, where Int[·] represents the integer portion. All these characteristics, in sharp contrast to conventional metals and other kinds of topological semimetals, should be experimentally observable.

Apart from the anomalous behavior of Landau level distribution, the Shubnikov–de Haas (SdH) oscillation of magnetic resistivity is another interesting magnetoresponse phenomenon in nodal-line semimetals, where the magnetoresistance oscillates periodically in reciprocal magnetic field $(1/B)$. Analysis of the SdH oscillations of magnetoresistance gives a nontrivial Berry phase, which is a distinct feature of nodal-line semimetals [74–77]. The oscillation of resistivity ρ under a magnetic field can be characterized by the Lifshitz-Kosevich formula

$$\rho \sim \cos\left[2\pi\left(\frac{F}{B} + \gamma\right)\right], \tag{19}$$

where B is the magnetic field. The frequency of oscillation $F = A\hbar/2\pi e$ is proportional to the extremal cross section area A on the Fermi surface that is normal to $\mathbf{B}$ [78]. The phase shift of the quantum oscillation is given by [79]

$$2\pi\gamma = -\pi + \phi_B \pm \frac{\pi}{8}, \tag{20}$$

which depends on the Berry phase ϕ_B acquired by winding along the extremal cyclotron orbit.

In a nodal-line semimetal, an electron can pick up a nontrivial π Berry phase around a loop that encloses the nodal line, while along the nodal ring the Berry phase is trivial. If the Fermi level is slightly away from the energy of the nodal ring, the Fermi surface becomes a torus [see Fig. 3(d)]. Therefore, there are multiple extremal cyclotron orbits which depend on the direction of magnetic field. As shown in Fig. 6(b), the outer (red) and inner (blue) orbits have maximum and minimum cross sections, respectively, in a perpendicular magnetic field $\mathbf{B}_\perp$. The Berry phase of the two orbits is zero. The nontrivial Berry phase of π appears when a parallel magnetic field $\mathbf{B}_\parallel$ is applied. Because there are two extremal orbits [yellow rings in Fig. 6(b)] that interlock with the nodal rings under $\mathbf{B}_\parallel$, a strong signature of the jump of the phase shift would be observed in the SdH oscillation if one tunes the magnetic field from $\mathbf{B}_\perp$ to $\mathbf{B}_\parallel$. In addition, due to the anisotropy of the torus Fermi surface, the extremal cross-section area A varies with the direction of magnetic field. Hence, a gradual modification of oscillatory frequency ($F = A\hbar/2\pi e$) would be measured when adjusting the direction of the magnetic field. As the nodal ring semimetal state can be effectively tuned by a uniaxial strain, the Landau levels as well as quantum oscillation would also be significantly modified by external strains.

IV. CONCLUSION

In summary, based on first-principles calculations and effective $k\cdot p$ model analysis, we discover that strained WC-type YN is an ideal topological semimetal with an ultraflat nodal ring when SOC is neglected. By applying a uniaxial strain, we can enlarge, shrink, and even annihilate the nodal ring, driving the system from a topological semimetal to a normal insulator. The tunability of the nodal ring in YN provides an alternative route for studying the topological phase transition of nodal-line semimetals. Furthermore, due to the ultraflat nodal-ring structure and a torus Fermi surface, YN exhibits anomalous Landau level structures and direction-dependent phase shifts of quantum oscillations. In addition, other novel physical features, such as an optical gap in the frequency-dependent conductivity due to Pauli blocking, are also expected to be observed in strained YN [34]. Therefore, our proposed YN with an ultraflat nodal ring also provides a prototype material to investigate the exotic physical properties of nodal-ring semimetals.

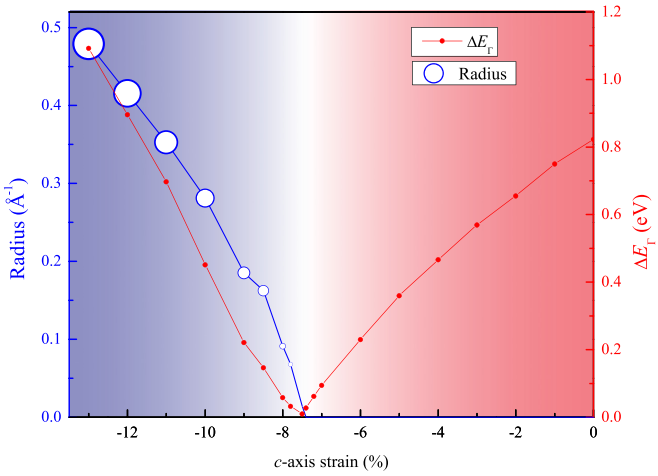

FIG. 7. The radius of the nodal ring and the energy gap at Γ (ΔE_Γ) as a function of uniaxial strain along the c axis. The calculations are carried out using the HSE06 hybrid functional.

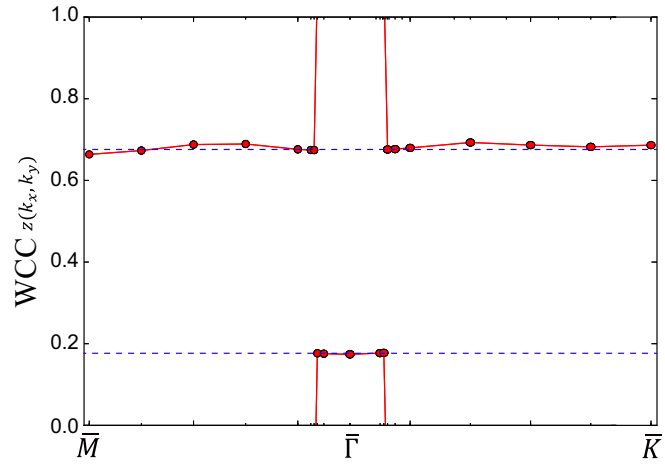

FIG. 8. Evolution of the total WCC of YN in the absence of SOC. The total WCC $z(k_x, k_y)$ jumps by a step of 0.5 when passing through the projected nodal ring from the outside to the inside around the $\bar{\Gamma}$ point. This jump corresponds to a Berry phase of π and a nontrivial topological invariant $\zeta_1 = 1$.

ACKNOWLEDGMENTS

This work was supported by U.S. DOE-BES (Grant No. DE-FG02-04ER46148). The calculations were done on the CHPC at the University of Utah and DOE-NERSC.

APPENDIX A: HYBRID FUNCTIONAL CALCULATIONS OF THE STRAIN EFFECT ON YN

We checked the strain effect using the nonlocal Heyd-Scuseria-Ernzerhof (HSE06) hybrid functional calculation [47,48]. As shown in Fig. 7, the phase transition occurs under a compressive strain of about −7.5%. It is noted that the tunability of electronic structures of YN can still be controlled by external strains, and the unique ultraflat feature of the nodal ring remains in the semimetal region. Therefore, the anomalous Landau level distribution and direction-dependent phase shifts of quantum oscillation are also observable in this phase.

APPENDIX B: CALCULATION OF TOPOLOGICAL INVARIANT ζ_1

To understand the nontrivial topological nature of YN, thus elucidating the structure of the topological surface states, the topological invariant ζ_1 in Eq. (15) is computed from a Wannier-based tight-binding Hamiltonian obtained from the first-principles calculation. Instead of directly calculating the Berry connection $\mathcal{A}(\mathbf{k})$, we adopt an equivalent but more effective way to calculate the topological invariant, i.e., tracing the evolution of 1D hybrid Wannier charge centers (WCC) [80] during a "time-reversal pumping" process [81].

In the following, we review the method that enables us to calculate the topological invariant of a general 2D insulator or 2D plane in the 3D Brillouin zone. The 1D hybrid Wannier functions (WFs) localized in the z direction are constructed as

$$|W_{nR_z}(k_x, k_y)\rangle = \frac{1}{2\pi}\int_0^{2\pi} dk_z e^{ik_z(r_z - R_z)}|u_n(\mathbf{k})\rangle, \qquad \text{(B1)}$$

where R_z is the z component of a lattice vector $\mathbf{R}$ and $|u_n(\mathbf{k})\rangle$ is the cell-periodic part of the Bloch wave function. The hybrid WCC $\langle z_n\rangle(k_x, k_y)$ is then defined as the expectation value of $\hat{z}$ for the hybrid WFs in the "home" unit cell $R_z = 0$, i.e., $\langle z_n\rangle(k_x, k_y) = \langle W_{n0}|\hat{z}|W_n 0\rangle$. For the nodal-line semimetal states in the absence of SOC, the sum $z(k_x, k_y) = \sum_n \langle z_n\rangle(k_x, k_y)$ over occupied bands would jump by a step of 1/2 when passing through the projected nodal ring in the k_x-k_y plane, which corresponds to a Berry phase $\phi_B = \pi$ for any loops winding around this nodal line in momentum space. Therefore, this method gives a simple and direct way to comprehend the topology of the whole occupied subspace.

For a spinless system respecting both time-reversal and inversion symmetries, the Berry phase has to be either zero or π for an arbitrary loop in the BZ. Therefore, we expect that the total hybrid WCC $z(k_x, k_y)$ will be quantized as either 0 or 1/2 at any (k_x, k_y) and that $z(k_x, k_y)$ will jump by 1/2 when passing through a projected nodal point. As YN does not possess inversion symmetry, $z(k_x, k_y)$ is no longer quantized as either 0 or 1/2. However, the sudden jump of 1/2 will still appear when going through the projected nodal ring, which indicates that the topological invariant $\zeta_1 = 1$ is nontrivial, as shown in Fig. 8. Our calculation of the topological invariant indicates the nontrivial electronic topology of the bulk bands and the existence of topological surface states on the surfaces of the nodal-line semimetal.

[1] M. Z. Hasan and C. L. Kane, Rev. Mod. Phys. **82**, 3045 (2010).
[2] X.-L. Qi and S.-C. Zhang, Rev. Mod. Phys. **83**, 1057 (2011).
[3] Z. Wang, Y. Sun, X.-Q. Chen, C. Franchini, G. Xu, H. Weng, X. Dai, and Z. Fang, Phys. Rev. B **85**, 195320 (2012).

[4] Z. Wang, H. Weng, Q. Wu, X. Dai, and Z. Fang, Phys. Rev. B **88**, 125427 (2013).

[5] H. Weng, C. Fang, Z. Fang, B. A. Bernevig, and X. Dai, Phys. Rev. X **5**, 011029 (2015).

[6] S.-M. Huang, S.-Y. Xu, I. Belopolski, C.-C. Lee, G. Chang, B. Wang, N. Alidoust, G. Bian, M. Neupane, C. Zhang, S. Jia, A. Bansil, H. Lin, and M. Z. Hasan, Nat. Commun. **6**, 7373 (2015).

[7] H. Huang and F. Liu, Phys. Rev. B **95**, 201101 (2017).

[8] A. A. Soluyanov, D. Gresch, Z. Wang, Q. Wu, M. Troyer, X. Dai, and B. A. Bernevig, Nature (London) **527**, 495 (2015).

[9] K. Deng, G. Wan, P. Deng, K. Zhang, S. Ding, E. Wang, M. Yan, H. Huang, H. Zhang, Z. Xu, J. Denlinger, A. Fedorov, H. Yang, W. Duan, H. Yao, Y. Wu, S. Fan, H. Zhang, X. Chen, and S. Zhou, Nat. Phys. **12**, 1105 (2016).

[10] H. Huang, S. Zhou, and W. Duan, Phys. Rev. B **94**, 121117 (2016).

[11] M. Yan, H. Huang, K. Zhang, E. Wang, W. Yao, K. Deng, G. Wan, H. Zhang, M. Arita, H. Yang, Z. Sun, H. Yao, Y. Wu, S. Fan, D. Wenhui, and S. Zhou, Nat. Commun. **8**, 257 (2017).

[12] T.-R. Chang, S.-Y. Xu, D. S. Sanchez, W.-F. Tsai, S.-M. Huang, G. Chang, C.-H. Hsu, G. Bian, I. Belopolski, Z.-M. Yu, S. A. Yang, T. Neupert, H.-T. Jeng, H. Lin, and M. Z. Hasan, Phys. Rev. Lett. **119**, 026404 (2017).

[13] H. Huang, K.-H. Jin, and F. Liu, arXiv:1711.07096.

[14] S. Li, Z.-M. Yu, Y. Liu, S. Guan, S.-S. Wang, X. Zhang, Y. Yao, and S. A. Yang, Phys. Rev. B **96**, 081106 (2017).

[15] X. Zhang, L. Jin, X. Dai, and G. Liu, J. Phys. Chem. Lett. **8**, 4814 (2017).

[16] T.-R. Chang, I. Pletikosic, T. Kong, G. Bian, A. Huang, J. Denlinger, S. K. Kushwaha, B. Sinkovic, H.-T. Jeng, T. Valla, W. Xie, and R. J. Cava, arXiv:1711.09167.

[17] J. He, X. Kong, W. Wang, and S.-P. Kou, arXiv:1709.08287.

[18] H. Huang, K.-H. Jin, S. Zhang, and F. Liu, Nano Lett. **18**, 1972 (2018).

[19] R. Okugawa and S. Murakami, Phys. Rev. B **96**, 115201 (2017).

[20] T. Hyart, R. Ojajärvi, and T. Heikkilä, J. Low Temp. Phys., **191**, 35 (2017).

[21] X. Feng, C. Yue, Z. Song, Q. Wu, and B. Wen, Phys. Rev. Mater. **2**, 014202 (2018).

[22] Y. Kim, B. J. Wieder, C. L. Kane, and A. M. Rappe, Phys. Rev. Lett. **115**, 036806 (2015).

[23] R. Yu, H. Weng, Z. Fang, X. Dai, and X. Hu, Phys. Rev. Lett. **115**, 036807 (2015).

[24] X.-L. Sheng, Z.-M. Yu, R. Yu, H. Weng, and S. A. Yang, J. Phys. Chem. Lett. **8**, 3506 (2017).

[25] T. Bzdušek, Q. Wu, A. Rüegg, M. Sigrist, and A. A. Soluyanov, Nature (London) **538**, 75 (2016).

[26] R. Yu, Q. Wu, Z. Fang, and H. Weng, Phys. Rev. Lett. **119**, 036401 (2017).

[27] C. Chen, Z. Su, X. Zhang, Z. Chen, and X.-L. Sheng, J. Phys. Chem. C **121**, 28587 (2017).

[28] Z. Yan, R. Bi, H. Shen, L. Lu, S.-C. Zhang, and Z. Wang, Phys. Rev. B **96**, 041103 (2017).

[29] P.-Y. Chang and C.-H. Yee, Phys. Rev. B **96**, 081114 (2017).

[30] W. Chen, H.-Z. Lu, and J.-M. Hou, Phys. Rev. B **96**, 041102 (2017).

[31] R. Bi, Z. Yan, L. Lu, and Z. Wang, Phys. Rev. B **96**, 201305 (2017).

[32] J. Wang, Y. Liu, K.-H. Jin, X. Sui, L. Zhang, W. Duan, F. Liu, and B. Huang, arXiv:1803.05235.

[33] J. Carbotte, J. Phys.: Condens. Matter **29**, 045301 (2016).

[34] S. Ahn, E. J. Mele, and H. Min, Phys. Rev. Lett. **119**, 147402 (2017).

[35] S. Barati and S. H. Abedinpour, Phys. Rev. B **96**, 155150 (2017).

[36] S. P. Mukherjee and J. P. Carbotte, Phys. Rev. B **95**, 214203 (2017).

[37] H. Yang, R. Moessner, and L.-K. Lim, Phys. Rev. B **97**, 165118 (2018).

[38] J.-W. Rhim and Y. B. Kim, Phys. Rev. B **92**, 045126 (2015).

[39] L.-K. Lim and R. Moessner, Phys. Rev. Lett. **118**, 016401 (2017).

[40] G. P. Mikitik and Y. V. Sharlai, Phys. Rev. B **97**, 085122 (2018).

[41] C. P. Kempter, N. Krikorian, and J. C. McGuire, J. Phys. Chem. **61**, 1237 (1957).

[42] A. Jain, S. P. Ong, G. Hautier, W. Chen, W. D. Richards, S. Dacek, S. Cholia, D. Gunter, D. Skinner, G. Ceder, and K. A. Persson, APL Mater. **1**, 011002 (2013).

[43] P. E. Blöchl, Phys. Rev. B **50**, 17953 (1994).

[44] G. Kresse and J. Furthmüller, Comput. Mater. Sci. **6**, 15 (1996).

[45] J. P. Perdew, K. Burke, and M. Ernzerhof, Phys. Rev. Lett. **77**, 3865 (1996).

[46] A. A. Mostofi, J. R. Yates, Y.-S. Lee, I. Souza, D. Vanderbilt, and N. Marzari, Comput. Phys. Commun. **178**, 685 (2008).

[47] J. Heyd, G. E. Scuseria, and M. Ernzerhof, J. Chem. Phys. **118**, 8207 (2003).

[48] J. Heyd and G. E. Scuseria, J. Chem. Phys. **120**, 7274 (2004).

[49] H. Huang, J. Liu, D. Vanderbilt, and W. Duan, Phys. Rev. B **93**, 201114 (2016).

[50] C. Fang, H. Weng, X. Dai, and Z. Fang, Chin. Phys. B **25**, 117106 (2016).

[51] H. Huang, K.-H. Jin, and F. Liu, Phys. Rev. B **96**, 115106 (2017).

[52] M. P. López Sancho, J. M. López Sancho, and J. Rubio, J. Phys. F **14**, 1205 (1984).

[53] M. P. López Sancho, J. M. López Sancho, and J. Rubio, J. Phys. F **15**, 851 (1985).

[54] H. Huang, Z. Wang, N. Luo, Z. Liu, R. Lü, J. Wu, and W. Duan, Phys. Rev. B **92**, 075138 (2015).

[55] Y. Sun, Y. Zhang, C.-X. Liu, C. Felser, and B. Yan, Phys. Rev. B **95**, 235104 (2017).

[56] C. Chen, X. Xu, J. Jiang, S.-C. Wu, Y. P. Qi, L. X. Yang, M. X. Wang, Y. Sun, N. B. M. Schröter, H. F. Yang, L. M. Schoop, Y. Y. Lv, J. Zhou, Y. B. Chen, S. H. Yao, M. H. Lu, Y. F. Chen, C. Felser, B. H. Yan, Z. K. Liu, and Y. L. Chen, Phys. Rev. B **95**, 125126 (2017).

[57] D. Takane, Z. Wang, S. Souma, K. Nakayama, C. X. Trang, T. Sato, T. Takahashi, and Y. Ando, Phys. Rev. B **94**, 121108 (2016).

[58] Y. Chen, Y.-M. Lu, and H.-Y. Kee, Nat. Commun. **6**, 6593 (2015).

[59] G. Bian, T.-R. Chang, R. Sankar, S.-Y. Xu, H. Zheng, T. Neupert, C.-K. Chiu, S.-M. Huang, G. Chang, I. Belopolski, D. S. Sanchez, M. Neupane, N. Alidoust, C. Liu, B. Wang, C.-C. Lee, H.-T. Jeng, C. Zhang, Z. Yuan, S. Jia, A. Bansil, F. Chou, H. Lin, and M. Z. Hasan, Nat. Commun. **7**, 10556 (2016).

[60] G. Bian, T.-R. Chang, H. Zheng, S. Velury, S.-Y. Xu, T. Neupert, C.-K. Chiu, S.-M. Huang, D. S. Sanchez, I. Belopolski, N. Alidoust, P.-J. Chen, G. Chang, A. Bansil, H.-T. Jeng, H. Lin, and M. Z. Hasan, Phys. Rev. B **93**, 121113 (2016).

[61] H. Weng, C. Fang, Z. Fang, and X. Dai, Phys. Rev. B **93**, 241202 (2016).

[62] H. Weng, C. Fang, Z. Fang, and X. Dai, Phys. Rev. B **94**, 165201 (2016).
[63] Z. Zhu, G. W. Winkler, Q. S. Wu, J. Li, and A. A. Soluyanov, Phys. Rev. X **6**, 031003 (2016).
[64] Y. Zhou, P. Lu, Y. Du, X. Zhu, G. Zhang, R. Zhang, D. Shao, X. Chen, X. Wang, M. Tian, J. Sun, X. Wan, Z. Yang, W. Yang, Y. Zhang, and D. Xing, Phys. Rev. Lett. **117**, 146402 (2016).
[65] Z. Guo, P. Lu, T. Chen, J. Wu, J. Sun, and D. Xing, Sci. China: Phys., Mech. Astron. **61**, 038211 (2018).
[66] J. Wang, X. Sui, W. Shi, J. Pan, S. Zhang, F. Liu, S.-H. Wei, Q. Yan, and B. Huang, Phys. Rev. Lett. **119**, 256402 (2017).
[67] H. Huang, K.-H. Jin, and F. Liu, Phys. Rev. Lett. **120**, 136403 (2018).
[68] H. B. Nielsen and M. Ninomiya, Phys. Lett. B **130**, 389 (1983).
[69] C.-L. Zhang, S.-Y. Xu, I. Belopolski, Z. Yuan, Z. Lin, B. Tong, G. Bian, N. Alidoust, C.-C. Lee, S.-M. Huang, T.-R. Chang, G. Chang, C.-H. Hsu, H.-T. Jeng, M. Neupane, D. S. Sanchez, H. Zheng, J. Wang, H. Lin, C. Zhang, H.-Z. Lu, S.-Q. Shen, T. Neupert, M. Z. Hasan, and S. Jia, Nat. Commun. **7**, 10735 (2016).
[70] J. Xiong, S. K. Kushwaha, T. Liang, J. W. Krizan, M. Hirschberger, W. Wang, R. J. Cava, and N. P. Ong, Science **350**, 413 (2015).
[71] C.-Z. Li, L.-X. Wang, H. Liu, J. Wang, Z.-M. Liao, and D.-P. Yu, Nat. Commun. **6**, 10137 (2015).
[72] H. Li, H. He, H.-Z. Lu, H. Zhang, H. Liu, R. Ma, Z. Fan, S.-Q. Shen, and J. Wang, Nat. Commun. **7**, 10301 (2016).
[73] Q. Li, D. E. Kharzeev, C. Zhang, Y. Huang, I. Pletikosić, A. Fedorov, R. Zhong, J. Schneeloch, G. Gu, and T. Valla, Nat. Phys. **12**, 550 (2016).
[74] K. S. Novoselov, A. K. Geim, S. Morozov, D. Jiang, M. Katsnelson, I. Grigorieva, S. V. Dubonos, and A. Firsov, Nature (London) **438**, 197 (2005).
[75] Y. Zhang, Y.-W. Tan, H. L. Stormer, and P. Kim, Nature (London) **438**, 201 (2005).
[76] L. P. He, X. C. Hong, J. K. Dong, J. Pan, Z. Zhang, J. Zhang, and S. Y. Li, Phys. Rev. Lett. **113**, 246402 (2014).
[77] J. Cao, S. Liang, C. Zhang, Y. Liu, J. Huang, Z. Jin, Z.-G. Chen, Z. Wang, Q. Wang, J. Zhao, S. Li, X. Dai, J. Zou, Z. Xia, L. Liang, and F. Xiu, Nat. Commun. **6**, 7779 (2015).
[78] L. Onsager, Philos. Mag. **43**, 1006 (1952).
[79] C. Li, C. M. Wang, B. Wan, X. Wan, H.-Z. Lu, and X. C. Xie, Phys. Rev. Lett. **120**, 146602 (2018).
[80] N. Marzari and D. Vanderbilt, Phys. Rev. B **56**, 12847 (1997).
[81] A. A. Soluyanov and D. Vanderbilt, Phys. Rev. B **83**, 235401 (2011).